

High power gamma flare generation in multi-petawatt laser interaction with tailored targets

K.V. Lezhnin,^{1,2} P. Sasorov,^{3,4} G. Korn,⁴ and S.V. Bulanov^{4,5,6}

¹*Department of Astrophysical Sciences, Princeton University, Princeton, New Jersey 08544, USA*

²*National Research Nuclear University MEPhI, Moscow 115409, Russia*

³*Keldysh Institute of Applied Mathematics RAS, Moscow 125047, Russia*

⁴*Institute of Physics ASCR, v.v.i. (FZU), ELI-Beamlines Project, Prague 182 21, Czech Republic*

⁵*National Institutes for Quantum and Radiological Sciences and Technology, KPSI, Kyoto 619-0215, Japan*

⁶*Prokhorov General Physics Institute, Russian Academy of Sciences, Moscow 119991, Russia*

(Dated: September 26, 2018)

Using quantum electrodynamics particle-in-cell simulations, we optimize the gamma flare (γ -flare) generation scheme from interaction of high power petawatt-class laser pulse with tailored cryogenic hydrogen target having extended preplasma corona. We show that it is possible to generate an energetic flare of photons with energies in the GeV range and total flare energy being on a kilojoule level with an efficient conversion of the laser pulse energy to γ -photons. We discuss how the target engineering and laser pulse parameters influence the γ -flare generation efficiency. This type of experimental setup for laser-based γ source would be feasible for the upcoming high power laser facilities. Applications of high intensity γ ray beams are also discussed.

I. INTRODUCTION

In recent years, high power laser technology has reached the level of petawatt (PW) scale with kilojoule (kJ) laser pulse energy [1–3]. Currently, ELI L4, a 10 PW, 1.5 kJ laser is being built at the ELI-Beamlines facility [4], while the proposals for even higher laser pulse power facilities are announced. High power laser-matter interaction results in generation of high energy beams of charged particles, electrons and ions, photons in a wide frequency range spanning from low-frequency electromagnetic pulses to γ -rays. At high energy end, irradiation of plasma targets by high-intensity laser leads to manifestation of nonlinear Thomson and Compton scattering processes, causing emission of photons with energies up to hundred MeV-scale, which is in γ range. Generation of high power γ -flares is thought to be one of a primary goals for high power laser facilities, [4–8]. Laser-based γ ray source may be applicable in radiation chemistry and material sciences [9, 10], in medicine in such a concept like ‘gamma knife’ [11, 12], in nuclear physics, where γ -rays will help to excite isotopes [13] for further use, as well as for laboratory astrophysics [14] research, testing theories on astrophysical gamma ray bursts generation [15, 16] and behaviour of a quantum electrodynamics (QED) plasma in pulsar magnetospheres [17].

As theoretically foreseen, an irradiation of plasma targets by multi-petawatt laser radiation can result in high efficiency of the laser energy conversion to the energy of gamma-ray flash [18–28]. Below, we present the results of multi-parametric studies of laser-target interaction for generation of bright γ -flare, aiming on parameters of ≈ 10 PW, kJ-scale laser, which will be available in the coming years. Using quasi-classical fully kinetic relativistic 2D and 3D QED PIC simulations with the code EPOCH [29], we find a regime where a significant fraction of laser pulse energy may be converted to γ -rays by optimizing

both preplasma and laser pulse. We show how target and laser parameters influence the γ ray generation, specifying energy spectrum and angular distribution of low and high-energy photons. We provide analytical estimates for manifestation of Compton scattering processes in an underdense plasma medium and discuss its physics in detail.

The paper is organized as follows. In Section II, we reveal known properties of the nonlinear Thomson scattering and Compton scattering mechanisms of the γ photon generation, which further will be used. Then, in Section III, we formulate a numerical setup for our 2D and 3D QED PIC simulations. In Section IV, we discuss the simulation results and provide details of γ -flare optimization. In Section VI, analytical expressions for the inverse Compton scattering in a medium are derived. Finally, in Section VII, we restate our main findings and discuss further direction of the γ -flare generation research.

II. NONLINEAR THOMSON SCATTERING AND COMPTON SCATTERING MECHANISMS OF GAMMA PHOTON GENERATION

In the case of tight focusing of 10 PW laser pulses, the field intensity can reach values up to 10^{24} W/cm² corresponding to normalized field amplitude $a_0 = eE/m_e\omega_0c \approx 10^3$, with e , E , m_e , ω_0 , and c being an elementary charge, electric field amplitude, electron mass, frequency of laser pulse, and speed of light in vacuum, respectively. This field amplitude is already enough for radiation reaction friction force to become dominant, as $a_0\varepsilon_{\text{rad}}^{1/3} > 1$. Here the parameter $\varepsilon_{\text{rad}} = 4\pi r_e/3\lambda$ characterizes the radiation friction effects; $r_e = e^2/m_e c^2 \approx 2.8 \times 10^{-13}$ cm is the classical electron radius and λ is the laser pulse wavelength (see [14, 30] and references cited therein). The normalized field amplitude $a_0 = \varepsilon_{\text{rad}}^{-1/3}$

for $\lambda = 1\mu\text{m}$ corresponds to the radiation intensity $\approx 10^{23} \text{ W/cm}^2$. The energy of photons emitted by ultrarelativistic electrons via the nonlinear Thomson scattering mechanism $\hbar\omega_\gamma$ is proportional to the cube of the electron energy,

$$\hbar\omega_\gamma \approx 0.3\hbar\omega_0 a_0^3. \quad (1)$$

For $a_0 \approx 200$ it is in γ -ray range.

In the interval of laser amplitudes $1 < a_0 < \varepsilon_{\text{rad}}^{-1/3}$ the nonlinear Thomson scattering cross section grows as $\sigma_{\text{NTS}} = \sigma_{\text{T}}(1 + a_0^2)$. Then at $a_0 \approx 1.1\varepsilon_{\text{rad}}^{-1/3}$ the radiation friction effects limit the cross section by the maximal value $\sigma_{\text{NTS}} = 0.53\sigma_{\text{T}}\varepsilon_{\text{rad}}^{-2/3}$. For $a_0 > \varepsilon_{\text{rad}}^{-1/3}$, the cross section decreases as $\sigma_{\text{NTS}} = \sigma_{\text{T}}/a_0\varepsilon_{\text{rad}}$ (for details see Ref. [14]). Here, $\sigma_{\text{T}} = (8\pi/3)r_e^2 = 6.65 \times 10^{-25} \text{ cm}^2$ is the Thomson scattering cross section.

The gamma-rays, generated in laser plasmas due to the nonlinear Thomson scattering, were observed experimentally (see Refs. [31–33]). The bremsstrahlung mechanism can also generate the gamma-rays in this situation [34–39]. However, the nonlinear Thomson and Compton effects are considerably more effective under conditions, discussed below.

When the energy of the photon emitted according to Eq. (1) becomes equal to the electron energy, the recoil effect cannot be neglected. Taking the electron energy to be equal to $m_e c^2 a_0$ we find from Eq. (1) that quantum regime starts at the laser amplitude above $\sqrt{m_e c^2 / \hbar\omega_0}$, i. e. at the intensity larger than $\approx 5 \times 10^{23} \text{ W/cm}^2$. The electron, colliding with the electromagnetic wave, in this case, emits the gamma photons in the nonlinear or multi-photon Compton scattering regime. The required intensity can be reached in the dense corona region, where the laser pulse undergoes the relativistic self-focusing, i.e. at later time of the laser-corona interaction.

At an order of magnitude higher intensity, i. e. at 10^{24} W/cm^2 , when the dimensionless parameter $\chi_e \approx \gamma_{e,0} a_0 / a_S$ becomes larger than unity, $\chi_e > 1$, such the QED effects as a recoil can play a significant role for a single electron interacting with the laser field. Here $\gamma_{e,0}$ is the electron gamma factor and normalized Schwinger field, $a_S = eE_S / m_e \omega_0 c$ with $E_S = m_e^2 c^3 / e\hbar$, is $a_S = m_e c^2 / \hbar\omega_0$. The gamma photon radiation mechanism in this limit is the nonlinear or multi-photon Compton scattering.

The one-photon Compton scattering cross section is given by the Klein-Nishina formula [40]. In ultrarelativistic limit, when the parameter

$$\kappa = \left(\frac{\hbar\omega_0}{m_e c^2} + \gamma_{e,0} \right)^2 - \left(\frac{\hbar\mathbf{k}_0}{m_e c} + \frac{\hbar\mathbf{p}_0}{m_e c} \right)^2 - 1 \quad (2)$$

is substantially larger than unity, total cross section is given by

$$\sigma_{\text{KN}} = 2\pi r_e^2 \frac{1}{\kappa} \left(\ln \kappa + \frac{1}{2} \right). \quad (3)$$

Here $p_{\parallel,0}$, $p_{\perp,0}$, and $\gamma_{e,0} = \sqrt{1 + p_{\parallel,0}^2 + p_{\perp,0}^2}$ are the longitudinal and perpendicular, along and perpendicular to electromagnetic wave propagation direction components of the electron momentum ($\mathbf{p}_0 = (p_{\parallel,0}, p_{\perp,0})$), and the electron gamma-factor before scattering, respectively. The photon frequency and wave-vector before scattering equal ω_0 and \mathbf{k}_0 . In nonrelativistic case, when $\kappa \ll 1$, i. e. the electron energy is less than 30 GeV, the Compton scattering cross section equals Thomson scattering cross section σ_{T} .

In the case of the Compton scattering on the electron in the field of the electromagnetic wave in vacuum, the dispersion equation for the wave frequency and wave vector takes the form $\omega^2 = \mathbf{k}^2 c^2$. In the ultra-relativistic limit, for $p_0 \gg m_e c$ the parameter κ given by Eq. (2) is approximately equal to $4\hbar\omega_0 p_{\parallel,0} / m_e^2 c^3$.

According to Eq. (1) an electron interacting with the electromagnetic wave emits high order harmonics. The maximum harmonic number could be equal to a_0^3 . In quantum physics this corresponds to the electron interaction with N_{ph} photons. Since an electron cannot emit the photon with the energy larger than the electron energy, $\hbar\omega_\gamma \leq m_e c^2 \gamma_e$, we obtain that the photon number is approximately equal to $N_{ph} = (m_e c^2 / \hbar\omega_0) a_0$. In this case, for $p_0 \gg m_e c$ the parameter κ becomes equal to $4N_{ph} \hbar\omega_0 p_{\parallel,0} / m_e^2 c^3 = a_0 p_{\parallel,0} / m_e c$.

The expression for the gamma ray photon energy can be found from the conservation of the energy and momentum in the photon-electron interaction:

$$\hbar\omega_\gamma = \frac{N_{ph} \hbar\omega_0 (p_{\parallel,0} c + m_e c^2 \gamma_{e,0})}{N_{ph} \hbar\omega_0 + m_e c^2 \gamma_{e,0} - p_{\perp,0} c \sin \theta + (\hbar\omega_0 - p_{\parallel,0} c) \cos \theta}, \quad (4)$$

i. e. in the expressions for one-photon Compton scattering $\hbar\omega_0$ should be replaced with $\hbar\omega_0 = m_e c^2 a_0$. The high energy γ -ray production in the multi-photon Compton scattering process has been observed in the experiments presented in Ref. [41]. For theoretical aspects of multi-photon Compton scattering see review articles [30, 42] and references therein. When the electron interacts with a plane electromagnetic wave of the amplitude a_0 we have $p_{\perp,0} = m_e c a_0$ and $p_{\parallel,0} = m_e c a_0^2 / 2$ (e. g. see Ref. [43]).

From Eq. (4) it follows that in the case of the head-on collision of the ultra-relativistic electron, $p_{\parallel,0} \gg m_e c$, with the electromagnetic pulse the maximum emitted photon energy is equal to $N_{ph} \hbar\omega_0 4(p_{\parallel,0} / m_e c)^2 \approx N_{ph} \hbar\omega_0 a_0^4$, provided $m_e c / 2p_{\parallel,0} = 1/a_0^2 \ll N_{ph} \hbar\omega_0 / m_e c^2$. It is equivalent to the condition $a_0 \ll \sqrt{m_e c^2 / N_{ph} \hbar\omega_0}$. In the case $a_0 \geq \sqrt{m_e c^2 / N_{ph} \hbar\omega_0}$ the γ -photon energy is approximately equal to $\hbar\omega_\gamma \approx p_{\parallel,0} c$. We see that in the limit $p_{\parallel,0} / m_e c \gg 1$ the gamma photons are emitted at the angle θ_a , which during a half of laser period changes from $\approx -2/a_0$ to $\approx +2/a_0$. In the receding configuration, for co-propagating electron and laser pulse the photon energy is well below the energy of incident photon, $N_{ph} \hbar\omega_0 / 4(p_{\parallel,0} / m_e c)^2$. As discussed below in

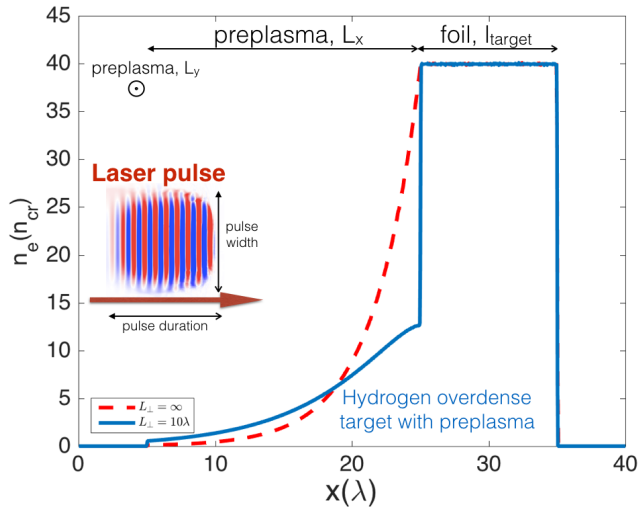


FIG. 1. Typical setup for 2D and 3D simulations. Target density profile averaged over transverse direction is shown for $L_{\perp} = \infty$ (red dashed line) and $L_{\perp} = 10\lambda$ (blue solid line).

Section VI the plasma effects changing the dispersion equation provide the conditions for high energy photon generation in the co-propagating configuration too.

Collective effects can make the threshold for the QED effects even lower, and, for laser pulses with $a_0 > 10^3$ interacting with plasma, in principle, a self-consistent model of QED plasma should be developed [30, 44].

III. SIMULATION SETUP

The Particle-In-Cell (PIC) simulations are performed with the relativistic electromagnetic code EPOCH [29], which includes QED processes. We perform a parametric scan with 2D version of the code, while also demonstrating results of the 3D simulation under the optimal conditions for γ -flare generation.

In the 2D runs, we consider p- and s-polarized Gaussian pulse with peak laser pulse power in the range from 1 to 20 PW. The pulse is incident on the target in the normal direction (it is along the x axis), being focused on the underdense corona preceding the high-density slab. We vary the pulse duration, from 5 fs to 150 fs, and the laser spot size from 1λ to 10λ . The optical axis of the laser pulse is at $y = 0$.

The cryogenic hydrogen target [46] comprises of two parts. The overdense slab with the uniform density of $40n_{\text{cr}}$ and thickness of l_{target} , varying from 1 to 20λ ($n_{\text{cr}} = m_e\omega^2/4\pi e^2$ is the plasma critical density). The preplasma corona is localized at the front side of the foil. It has exponential distribution of the density, proportional to

$$\exp\left(-\left(\frac{(x-x_0)^2}{L_{\parallel}^2} + \frac{(y-y_0)^2}{L_{\perp}^2}\right)\right).$$

Here (x_0, y_0) is a point on the front side surface of the

high-density hydrogen slab and L_{\parallel} and L_{\perp} are characteristic longitudinal and transverse scale-lengths of the corona density. We cut the corona at $0.1n_{\text{cr}}$, and fix the length of the preplasma in the x direction as $L_x = L_{\parallel} \times \ln(n_{\text{max}}/n_{\text{min}})$. In this expression, the maximum density equals $n_{\text{max}} = 40 n_{\text{cr}}$ and the minimum density n_{min} is chosen to be $0.1n_{\text{cr}}$. We vary the transverse scale length L_{\perp} from 1λ to ∞ . Preplasma at the front side of the high-density slab is assumed to be formed by the ASE pedestal or/and by the prepulse, which alter an initial density distribution of the target for such a high laser pulse power and finite laser pulse contrast. We choose the corona profile using the results of theoretical analysis of the preplasma corona formation presented in Ref. [45]. It is based on the hydrodynamics simulations conducted in order to describe the finite contrast effects on the laser ion acceleration by petawatt laser pulse. Our simulation setup is also similar to the setup used in Ref. [18], where a 2D PIC simulations were conducted in order to show a feasibility of the γ -flare generation. Our approach covers a broader range of parameters, and is based on a more fundamental numerical model of QED processes [47].

The length of a simulation box is $10\lambda + L_x + l_{\text{target}}$, which varies from 50λ to 110λ . The transverse size of the box is 60λ . We fix the number of grid points per λ to be equal to 20, while doing some simulations with 40 grid nodes per λ . We conduct a number of simulations varying the number of particles, which is typically $\{16, 32\} \times 2.64 \times 10^6$. Total simulation time is $(10\lambda + L_x + l_{\text{target}})/c + t_{\text{pulse}}$, ranging from 200 to 500 fs. Here, t_{pulse} is the pulse duration. Total energy error is less than 5% in all simulations. Initially, we don't have any photons in our simulation, but they are being generated throughout the simulation via the nonlinear Thompson and Compton scattering processes. The schematic of the simulation setup is shown in Figure 1.

To find an optimal regime for γ -flare generation with the maximum efficiency of laser pulse energy conversion to the energy of the γ -photon we vary the simulation parameters as follows. The peak laser pulse power is within the interval (1, 2.5, 5, 10, 20, and 40 PW). The pulse length equals 5, 10, 30, 50, and 150 fs. The laser pulse spot size, Δw is equal to 10, 5, 2.5, and 1λ . The laser pulse for 2D simulations has the s- and p- polarization. The thickness of the high density slab of the target, l_{target} is equal to 1, 5, 10, and 20λ . The preplasma length, L_x , equals 1, 5, 10, 20, 40, 80, 160λ , and the width, L_{\perp} , equals 1, 2.5, 5, 10, 20λ and ∞ , i.e. in this case the plasma density is homogeneous in the transverse direction.

We also conduct a series of auxiliary simulations in order to find whether or not a strongly focused 10 PW laser pulse is able to generate a fair amount of the γ -photon energy during the interaction with solid density slab. This case corresponds to the scheme proposed in Ref. [19].

In the case of 3D simulation, the parameters are as follows. We choose the simulation box size to be $70\lambda \times$

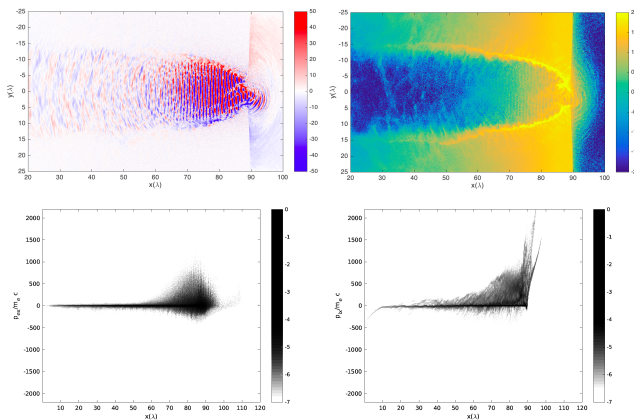


FIG. 2. a) Distribution of the z - component of magnetic field, b) Distribution of \log_{10} of electron density, c) electron $x - p_x$ phase plane, d) ion $x - p_x$ phase plane for $t = 400$ fs. Pulse self-focusing, hole boring, electron heating, and ion acceleration via RPDA/TNSA mechanisms.

$20\lambda \times 20\lambda$, with a grid resolution of 16 grid nodes per one λ . Total number of quasiparticles equals 1.84×10^9 . The laser pulse peak power is of 10 PW. The laser focal spot size, Δw , is 2.5λ . The pulse duration is of 50 fs. The laser is incident on the target along the x axis, centred around point $(y, z) = (0, 0)$. The laser pulse is linearly polarized, with the electric field directed along the y axis and the magnetic field along the z axis. Hydrogen target is 5λ thick, with preplasma size, L_x , equals to 10, 20, and 40λ and $L_\perp = \infty$. The simulation time equals 300 fs.

IV. PIC SIMULATION RESULTS

Let us first discuss the 2D QED PIC simulation results. Figure 2 shows a snapshot for $t = 400$ fs from the simulation with the conditions optimal in terms of the γ -flare generation. In this simulation run, the peak laser power is 10 PW, the laser pulse length equals 150 fs, the pulse width at the focus Δw is equal to 2.5λ . The radiation has p- polarization. The preplasma length in the longitudinal direction, L_x , is of 80λ . In the transverse direction the plasma density is homogeneous, $L_\perp = \infty$. The high-density slab thickness equals 5λ . As the width of the initial laser pulse is pretty small, $\lambda/\Delta w \approx 0.3$, the laser pulse diverges in transverse direction until it reaches a dense part of the preplasma, where it experiences the self-focusing. As a result it reaches the high-density part of the target being focused, with the width equal to $2-3\lambda$, Figure 2 a. A normalized amplitude of the laser pulse at the front side surface may be as high as $a_0 \approx 300$. Laser pulse bores a hole in the target and partially propagates through it, as seen on Figure 2 b. Though the parameters chosen are not optimal for the ion acceleration, we still observe in $x - p_x$ phase plane a relatively high energy proton beam (Figure 2 d). It can be formed as a result of the proton acceleration corresponding to Tar-

get Normal Sheath Acceleration (TNSA) [48] and/or the Radiation Pressure Acceleration (RPA) [49] mechanisms. In the $x - p_x$ electron phase plane in Figure 2c, the electron heating up to 0.5 GeV energy in the x -direction is seen. In opposite direction the electron energy is approximately equal to 125 MeV. The maximum kinetic energy of protons is around 600 MeV.

The angular distribution of photon energy is shown on Figure 3a(b) for $t = 180$ (400) fs. Figure 3c(d) shows distribution of the γ -photon density in the $x - y$ plane at the instant of time when the maximum photon energy is reached: $t = 180$ (400) fs. The main fraction of photon energy is shined in the laser pulse propagation direction. It is worth noting that during a first few tens of femtoseconds, when the laser pulse propagates in a very dilute plasma, the main fraction of the photon energy is directed *antiparallel* to the laser pulse propagation direction (Figure 3a). These photons can be understood as produced by scattering of laser pulse photons on a counterstreaming electrons, which try to circulate back along the self-focusing channel. Overall distribution of photon number may be considered almost isotropic, while the most energetic photons are emitted along the x axis (Figure 3b).

Figure 4 shows the energy spectrum of particles at $t = 400$ fs (Figure 4 a) and the energy evolution in a system throughout the simulation (Figure 4 b). We see that the preplasma allows us to almost completely absorb the laser pulse energy, leaving less than 10 % in the electromagnetic field energy, which may partially be contained by the quasistatic magnetic field in the laser pulse wake. As is known the quasistatic magnetic field is associated with the electron vortices [50]. In addition, not all the particle energy is converted into the γ -photon glow, as significant fraction is transformed into electron heating and ion acceleration (see Figures 2c, 2d, 4). However, for the parameters under discussion, the γ -flare optimization enables transforming 37% of the laser pulse energy into photons, with total γ ray energy as high as 450 J. Peak γ -flare power is around 3.8 PW. Comparison of photon and electron energy spectra shows that the emitted photon energies are approximately equal to electron energies. This fact underlines the importance of a discrete, QED radiation reaction effects, in such a laser-plasma interaction setup. We have conducted an auxiliary set of simulations with laser pulse focused onto a spot of 1λ scale at the front side of the solid hydrogen slab, which is similar to the configuration used in Ref. [19]. We have concluded that the energy conversion efficiency is less than 20% in the case of a relatively thick target with the thickness of 20λ .

V. RESULTS OF MULTI-PARAMETRIC SIMULATIONS

The results of multiparametric studies aimed at finding the maximal efficiency of the laser energy conversion

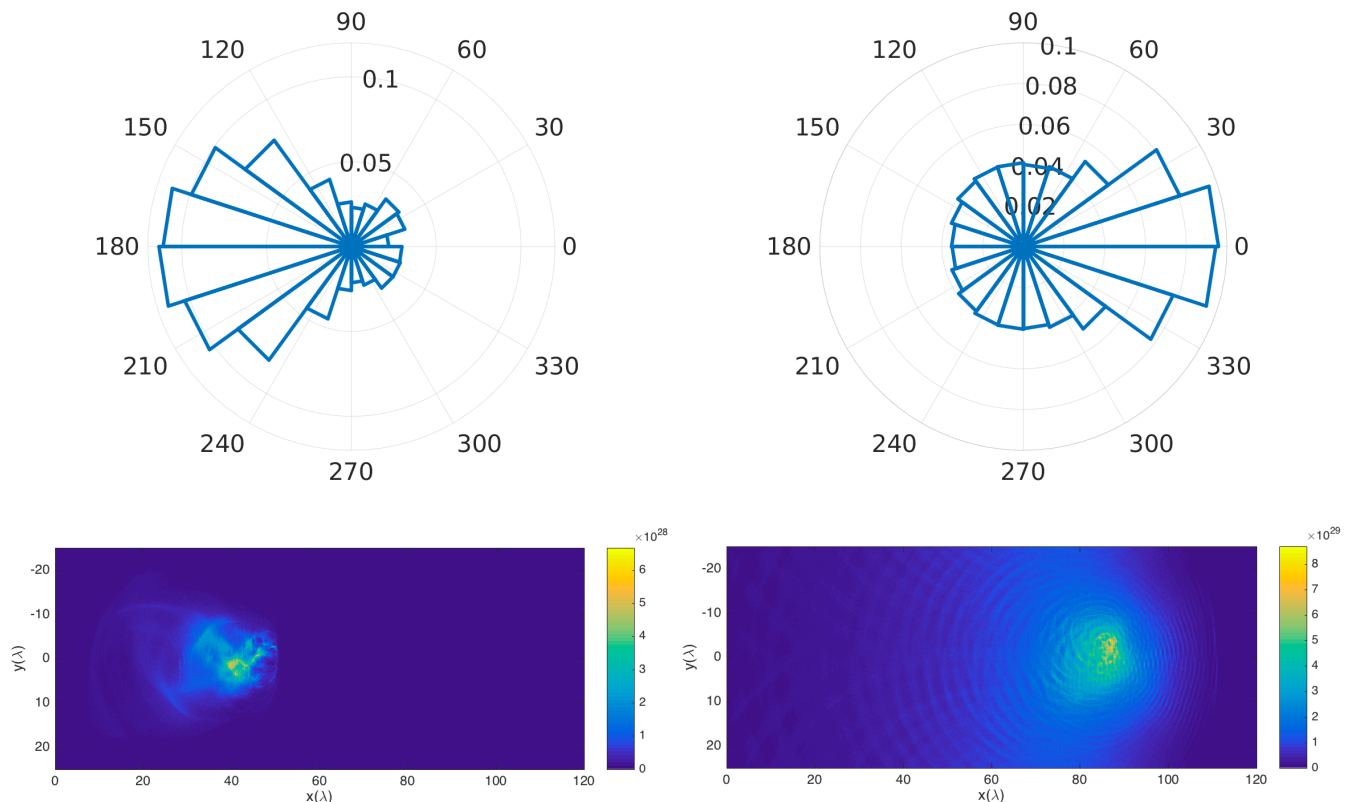


FIG. 3. Angular distribution of photon energy (a,b) and photon density distribution (c,d), at $t = 180$ fs (a,c) and $t = 400$ fs (b,d). Angular *particle number* distribution is isotropic, thus, most energetic photons are directed backwards during the first stages of interaction, while the most energetic particles in the whole simulation are directed forward.

to the γ flash energy are presented in Figure 5. Here the laser plasma interaction parameters are changed in a broad range. The preplasma corona length is a key importance parameter for providing the multi petawatt laser pulse damping. As it follows from the simulations of the laser interaction with solid hydrogen target without a preplasma corona and for the target with a preplasma corona short compared to the laser pulse length, the laser radiation is mostly reflected back. Typically approximately 50% of the laser is reflected, thus the γ flash generation occurs under far from the optimal conditions. On the other hand, a relatively long underdense corona in comparison to laser pulse length is also not optimal for the γ flash generation, since a large enough density gradient is required for efficient energy conversion. Auxiliary simulation with uniform density of $0.2n_{cr}$ shows a conversion efficiency less than 2% of laser pulse energy to photon energy. Apparently, there is an optimal preplasma length, which is required for bright γ radiation. The laser pulse length should also be long enough, as it is required for hole boring providing the conditions for high laser pulse to reach an optimal density gradient regions in the preplasma corona. The laser pulse width is in tight connection with preplasma conditions, as the relativistic self-focusing for narrow laser pulses will eventually focus to a dense overcritical regions of the preplasma

corona, where the laser-plasma interaction conditions are in agreement with estimates for an optimal laser power for efficient γ -flare, $\mathcal{P}_{las} \approx 10^2 \text{ PW} \cdot n_{cr}/n_e$, see [18, 51]. This condition yields that the 10 PW peak power of laser pulse should reach a overcritical density of $10n_{cr}$, which is indeed a time of peak power of γ -flare, according to Figure 4b.

Among other parameters, the high-density target thickness provides only a minor contribution to manipulating the energy conversion efficiency, as by the time when the laser pulse starts to bore a hole in the high-density part of the target the most portion of its energy is already depleted, see Figure 2a and red line on Figure 4b. However, a larger target still allows one to contain more heated electrons within the high-density slab, leading to a slightly higher efficiency of the γ -flare generation. The transverse scale length of the preplasma, L_{\perp} , is determined by the spot size of the prepulse, as shown by radiation hydrodynamics simulations presented in Ref. [45]. Usually, L_{\perp} is approximately equal to the focal spot size of the ASE pedestal. It can limit the γ -flare generation efficiency, according to the parametric scan shown in Figure 5e. The laser pulse power is certainly a very important parameter, as it controls how efficiently laser pulse can propagate in preplasma, boring a hole there. Lower the power is, over less distance the pulse

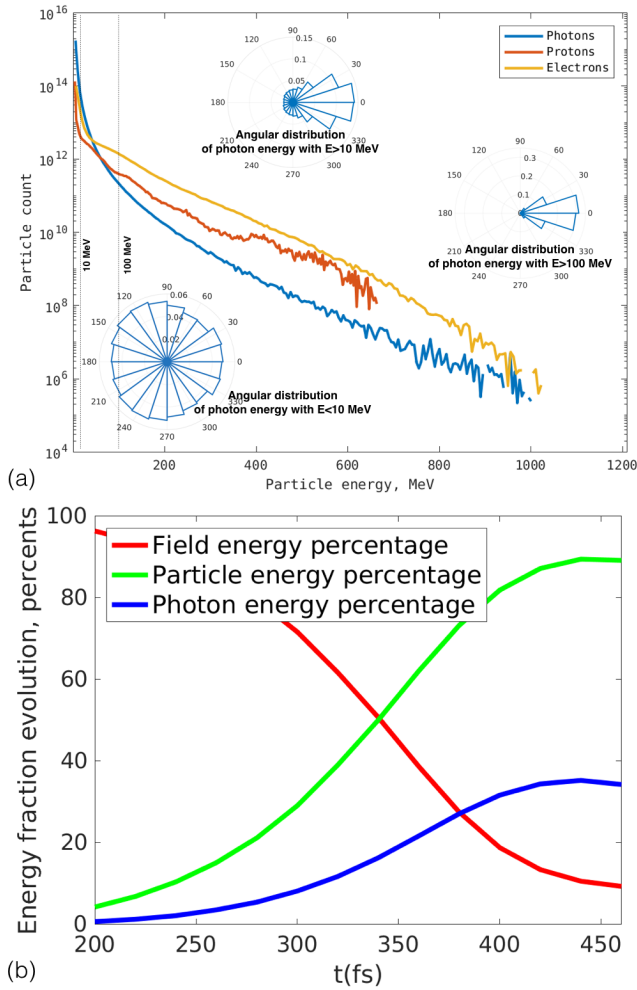


FIG. 4. a) Particle and photon energy spectra at $t = 400$ fs. Insets demonstrate an angular distribution of photon energy for photons with $\mathcal{E}_\gamma < 10$ MeV (bottom left), photons with $\mathcal{E}_\gamma > 10$ MeV (top center), and photons with $\mathcal{E}_\gamma > 100$ MeV (middle right). b) Particle, field, and photon energy evolution in the simulation.

propagates through the preplasma, never reaching its corresponding optimum for γ -flare generation. For example, for $\mathcal{P}_{\text{las}} = 2.5$ PW, the laser pulse should reach a $40n_{\text{cr}}$ region, but it is hard to do in the case of the target parameters used in the simulations.

Optimization of the preplasma profile for fixed 10 PW laser power allows one to obtain a 37% level of the laser energy conversion to the energy of γ -flare, which is slightly higher than it was obtained in previous 2D PIC simulations, where a simple model of photon generation has been used [18] with a simulation setup similar to the setup used in the present work. It is higher than the conversion efficiency found in previous 2D QED PIC simulations with EPOCH code [19], but with different target setup.

Apparently the conditions used for the gamma-ray generation are not optimal for electron-positron pair production, as we do not consider laser pulse fields larger than

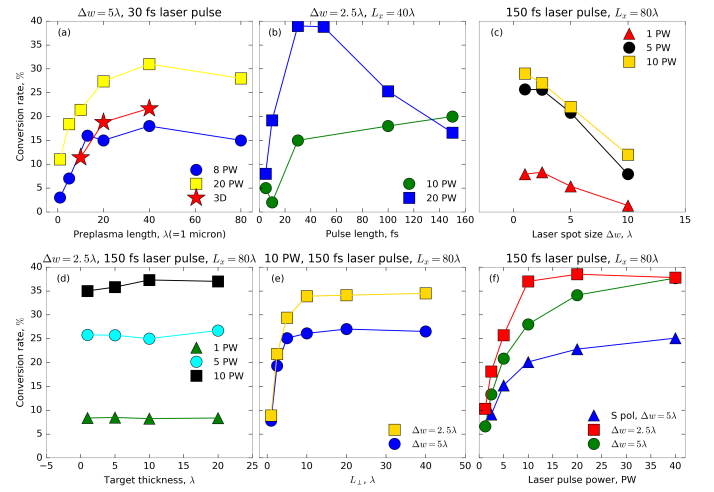


FIG. 5. Optimization of laser pulse and hydrogen target parameters for efficient energy conversion to γ -rays. Each circle, triangle, star, and square corresponds to a specific choice of the PIC simulation parameters. Fixing all the parameters but one and varying it we plot the conversion efficiency dependence on this parameter. The values of the parameters fixed in the simulation are written on each of the frames. Dependence of conversion efficiency on a) the preplasma length, in λ ; b) on laser pulse length for two peak laser pulse power values, c) on the laser spot size for two peak laser pulse power values, d) on the high-density slab thickness for two peak laser pulse power values, e) on L_\perp , which is an effective transverse width of the preplasma corona, for two laser spot size values, f) on laser pulse power for two laser spot size values.

$a_0 = 300$, while our additional simulations suggest that we need fields more than $a_{\text{pairs}} \approx 10^3$ in order to see pair formation, while its density is still low to make significant influence on the γ -flare parameters, in agreement with Ref. [19].

High-Z targets may be even more efficient in terms of enhancement of the gamma flare energy. As the simulations show, by keeping the same ion number density profile as in the optimal case, but for different target material, such as copper or gold with ionization degrees of 4 and 5, respectively, we can obtain an even higher energy conversion efficiency, up to 50%. For such the targets, the reaching of a peak gamma flare power corresponds to the time when the laser pulse interacts with the overdense preplasma region whose density is approximately equal to $10n_{\text{cr}}$. A detailed studying of such type of the targets will be considered in a separate paper.

Finally, Figure 6 shows a snapshot of 3D simulation, which demonstrates γ -photons (colored circles with color corresponding the photon energy), 2D cut of z component of the magnetic field through the $z = 0$ plane, and 2D cut of electron density through the $y = 0$ plane. In the $x = 0$ plane, an angular distribution of photon energy, with the y axis corresponding to θ angle changing from $-\pi$ to π and ϕ angle, from 0 to π . Cyan lines represent 1D cuts of the z -component of the magnetic field along

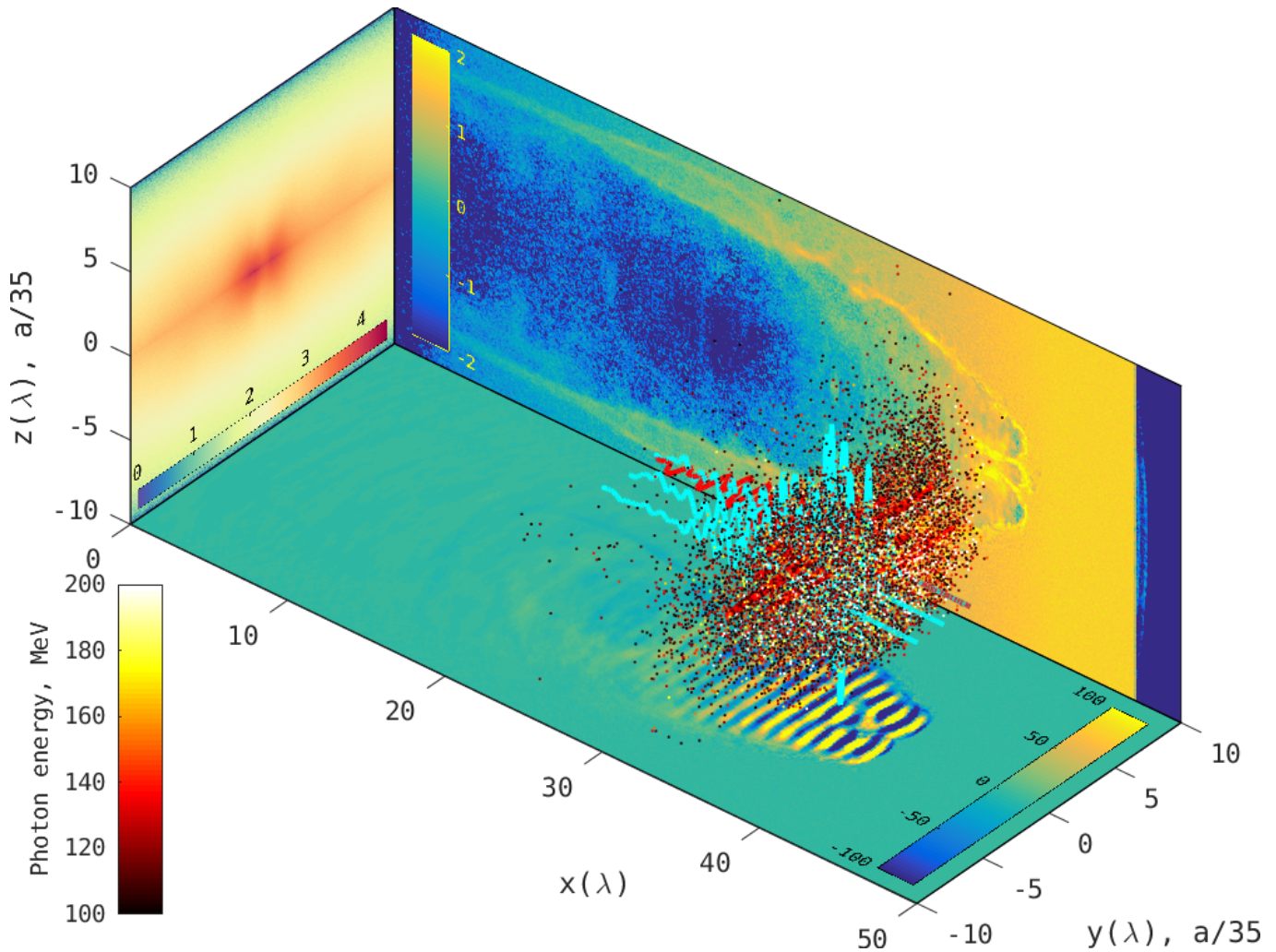


FIG. 6. Snapshot of the 3D QED PIC simulation results for preplasma length of $L_x = 40\lambda$, with \log_{10} of electron density distribution (in the $y = 10\lambda$ plane), the z component of the magnetic field (in the $z = -10\lambda$ plane), the angular distribution of \log_{10} photon energy (in the $x = 0$ plane), and the high energy photon distribution shown with the points whose color corresponds to photon energy. Cyan lines represent 1D cuts of the z component of the magnetic field along the lines $y = 0, z = 0$; $y = -2, z = 0$; $y = -4, z = 0$. Red line represents a 1D cut of the y component of the electric field along lines $y = 0, z = 0$. Colorbar shows a photon energy in MeV.

the lines $y = 0, z = 0$; $y = -2, z = 0$; $y = -4, z = 0$. Red line represents 1D cut of the y component of the electric field along the lines $y = 0, z = 0$. We plot only high-energy photons with $\mathcal{E}_\gamma > 100$ MeV. Their primary location is around the region where the peak laser pulse power is. Here the low electron density cavity is located. Energy conversion rate is less than in an ‘optimal’ case in 2D simulations, but still is a significant fraction of laser pulse energy, being no less than 20%. As in the case of 2D simulations, the majority of photon energy is directed forward along the laser pulse propagation direction. Photons are mainly confined within the cone with 60 degrees opening angle along the line $(y, z) = (0, 0)$, where around 60% of total photon energy is shined, see $x = 0$ plane of Figure 6. The 3D simulations also show that longer corona allows to reach a better gamma flare

generation efficiency.

VI. KINEMATICS OF INVERSE COMPTON SCATTERING IN COLLISIONLESS PLASMA

Gamma photons of a relatively low energy (1-10 MeV and less) are expected to be generated via the nonlinear Thomson scattering, when the energy of emitted photons $\hbar\omega_\gamma$ is proportional to the cube of the electron energy (see Eq. (1)).

Application of the theory of nonlinear Thomson scattering for high-efficiency gamma-ray generation has been discussed in details in Ref. [18], where it was shown that the optimal laser power scales with the electron density in the plasma corona as $10^2(\omega_0/\omega_{pe})^2$ PW. In the case

of the electron density approximately equal to $10 n_{cr}$, where the critical electron density is $n_{cr} = m_e \omega_0^2 / 4\pi e^2$, the required laser power is 10 PW.

As it is seen from Figures 2 and 4, at $t = 400$ fs the gamma-ray angular distribution has a form of a collimated beam directed along the direction of accelerated electrons and laser light propagation. If the electrons were interacting in vacuum with co-propagating electromagnetic wave one could not expect significant generation of high energy photons. The situation changes in the medium with the refraction index corresponding to collisionless plasmas. In the medium the Compton scattering acquires new features [53].

Here we consider a kinematics of the inverse multi-photon Compton scattering process in collisionless plasma of the near critical density when an ultra-relativistic electron collides with electromagnetic wave. By using the energy and momentum conservation in the electron-photon system we can find the scattering photon frequency dependence on the electron energy, the wave amplitude, the plasma density and the scattering angle. The energy conservation equates the sum of electron and N_{ph} photon energy before and after the scattering

$$m_e c^2 \gamma + \hbar \omega_\gamma = m_e c^2 \gamma_0 + N_{ph} \hbar \omega_0. \quad (5)$$

Here $\gamma_{e,0} = \sqrt{1 + (\mathbf{p}_0/m_e c)^2}$ and $\gamma_e = \sqrt{1 + (\mathbf{p}/m_e c)^2}$, \mathbf{p}_0 and \mathbf{p} , and ω_0 and ω_γ are the electron gamma factors, momenta, and photon frequency before and after collision, respectively. The momentum conservation yields

$$\mathbf{p} + \hbar \mathbf{k}_\gamma = \mathbf{p}_0 + N_{ph} \hbar \mathbf{k}_0, \quad (6)$$

where $\hbar \mathbf{k}_0$ and $\hbar \mathbf{k}_\gamma$ are the photon momentum before and after scattering on relativistic electron.

We assume that photon-electron interaction occurs in the (x, y) plane, i. e. $\mathbf{p}_0 = p_0 \mathbf{e}_x + m_e c a_0 \mathbf{e}_y$ and $\mathbf{p} = p_x \mathbf{e}_x + p_y \mathbf{e}_y$ with \mathbf{e}_x and \mathbf{e}_y being the unit vectors along the x - and y -axis, respectively, and $a_0 = eE_0/m_e \omega_0 c$ normalized field amplitude of the laser radiation, which is assumed to be linearly polarized with the electric field parallel to the y -axis.

In collisionless plasmas the electromagnetic wave frequency and wave number are related to each other as $\omega = \sqrt{\mathbf{k}^2 c^2 + \bar{\omega}_{pe}^2}$, where $\bar{\omega}_{pe} = \sqrt{4\pi n_e e^2 / m_e} \sqrt{1 + a_0^2}$ the plasma frequency (n_e is the electron number density) with relativistic effects taken into account according to Ref. [54].

Within the framework of the aforementioned assumptions by using Eqs. (5) and (6) and assuming that $\omega_0 = \bar{\omega}_{pe}$, i.e. the electron interacts with the electromagnetic wave in the critical density region, we find that the scattering cross section equals to that given by Eq. (3) with the parameter κ defined by Eq. (2) approximately equal to $2N_{ph} \hbar \omega_0 p_{||,0} / m_e^2 c^3$.

The energy of the gamma-photon generated in the

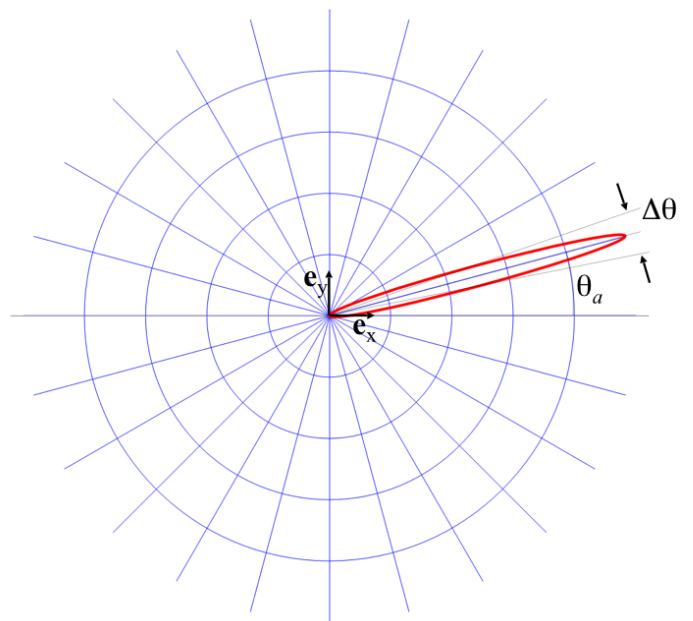


FIG. 7. Angular distribution of gamma-photons emitted at the angle θ_a and confined within the cone of the angle $\Delta\theta$.

Compton scattering process is given by

$$\hbar \omega_\gamma = \frac{N_{ph} \hbar \omega_0 (\hbar \omega_0 + m_e c^2 \gamma_{e,0})}{N_{ph} \hbar \omega_0 + m_e c^2 \gamma_{e,0} - p_{\perp,0} c \sin \theta - p_{||,0} c \cos \theta}. \quad (7)$$

Here θ is a scattering angle, i.e. $\mathbf{k}_\gamma = |\mathbf{k}_\gamma|(\mathbf{e}_x \cos \theta + \mathbf{e}_y \sin \theta)$. We see from Eq. (7) that in the limit $p_{||,0}/m_e c \gg 1$ and $p_{\perp,0} = m_e c a_0$ the gamma photons are emitted at the angle θ_a , which during a half of laser period it changes from $\approx -a_0/p_{||,0}$ to $\approx +a_0/p_{||,0}$ being confined within the cone $\Delta\theta \approx \sqrt{(1 + a_0^2)m_e^2 c^2 / p_{||,0}^2 + N_{ph} \hbar \omega_0 / m_e c^2}$. The angular dependence of the γ photons, when their distribution is elongated according to the laser pulse polarization has been observed in the experiment presented in Ref. [33]. It is also well seen in Fig. 7.

The maximum gamma photon energy is approximately equal to $N_{ph} \hbar \omega_0 2(p_{||,0}/m_e c)^2$ provided $p_{||,0}/m_e c \ll m_e c^2 / 2N_{ph} \hbar \omega_0$. Otherwise, for $p_{||,0}/m_e c \gg m_e c^2 / 2N_{ph} \hbar \omega_0$ the gamma photon energy is about $\hbar \omega_\gamma \approx m_e c^2 \gamma_{e,0}$, which is a typical case for the parameters under the consideration - these photons may obtain energies up to GeV level.

VII. CONCLUSIONS AND DISCUSSIONS

In this paper, the optimization of laser-plasma interaction parameters for efficient γ -flare generation, in terms of both laser pulse energy conversion to γ -rays and γ -flare power are discussed. The multiparametric analysis based on the using 2D and 3D QED PIC code EPOCH

shows how the laser pulse and preplasma parameters are related to the γ radiation from the laser irradiated target. Typical target under consideration comprises the solid density hydrogen slab with the near-critical density inhomogeneous preplasma corona. The corona length is approximately equal to the laser pulse length, i. e. it is typically in the interval from $10\mu\text{m}$ to $50\mu\text{m}$. For such the corona plasma parameters the bremsstrahlung energy losses of ultrarelativistic electrons are negligibly weak. The electrons lose the energy here in the form of the high-energy photons. The photon radiation mechanism is the nonlinear Thomson scattering, and at the electron high energy end the γ -photons are emitted via the multi-photon Compton scattering with the photon number $N_{ph} \gg 1$.

The simulations provide an information on the angular distribution of photon energies in different energy bands. It is shown that the low-energy γ -photons with energies less than 10 MeV are distributed isotropically, while the high energy photons are directed mainly in the direction of laser pulse propagation. Maximum energy of photons may reach a GeV energy level. In the process of high energy photon generation in the co-propagation electron-electromagnetic wave configuration the crucial role is played by the fact that the group velocity of the laser pulse in the near-critical density region becomes substantially less than the speed of light in vacuum. As we may see from Eq. (7) in this case the high energy photons can be generated in both the electron-photon co-propagation and counter-propagation configurations. This is in contrast with the electron-photon interaction described by Eq. (4).

Regarding the ion acceleration for the laser-target parameters under discussion, it occurs to be in a non-optimal regime, as we seek for conditions to maximize the energy conversion to γ -photons. However, the ion acceleration up to 600 MeV is seen via a combination of the RPA and TNSA acceleration mechanisms. Electron heating is also seen, up to GeV level. Analyzing the electron and photon energy spectra, we may conclude that

with the 10 PW pulse laser, the QED radiation reaction regime can be reached, where radiation reaction affects the electron dynamics by emitting discrete photons with energies up to the electron energy, rather than its classical version of continuous radiation.

The 3D simulations prove the conceptual feasibility to generate a bright γ -flare, with energy conversion rate of around 20%, which is in agreement with our 2D simulations with corresponding laser pulse and target parameters.

Our findings open a way towards various applications of ultra-short pulse high power γ ray sources. Among them one of the most attractive is the material sciences allowing one to extend the radiation chemistry [9, 10] to the regimes when ultra-relativistic physical processes come into play. In the GeV gamma-ray energy range the gamma-rays are absorbed in the media via the electron-positron pair generation [55] with the cross section approximately equal to 10 barns. In contrast with other γ ray sources, in the case of the laser generated γ -rays, the flash duration is in the femtosecond to picosecond interval.

VIII. ACKNOWLEDGEMENTS

Computational resources were provided by the ECLIPSE cluster of ELI-Beamlines. The EPOCH code was developed as part of the UK EPSRC funded projects EP/G054940/1. At ELI-BL, the work has been supported by the project High Field Initiative (CZ.02.1.01/0.0/0.0/15.003/0000449) from the European Regional Development Fund. KVL is grateful to ELI-Beamlines project for hospitality during this work. Authors are thankful to T. Zh. Esirkepov, V. Istoksaika, J. Koga, K. Kondo, M. Kando, T. Kawachi, D. Margarone, K. Nishihara, F. Schillaci, S. Singh, K. Tanaka, and W. Yan for useful discussions and to Y. J. Gu, D. R. Khikhlukha, E. Chacon-Golcher, and M. Matys for assistance with computer simulations.

-
- [1] C. Danson, D. Hillier, N. Hopps, and D. Neely, *High Power Laser Science and Engineering* **3**, 14 (2015).
 - [2] N. Miyanaga, H. Azechi, T. Kanabe, T. Jitsuno, K. Kondo, Y. Fujimoto, N. Morio, S. Matsuo, Y. Kawakami, R. Mizoguchi, K. Tauchi, M. Yano, S. Kudo, Y. Ogura, *J. Phys. Conf. Ser.* **112**, 032006 (2008).
 - [3] Y. Arikawa, S. Kojima, A. Morace, et al., *Appl. Opt.* **55**, 6850 (2016).
 - [4] ELI-Extreme Light Infrastructure Science and Technology with Ultra-Intense Lasers Whitebook, Ed. by G. A. Mourou, G. Korn, W. Sandner, and J. L. Collier (THOSS Media, Berlin, 2011).
 - [5] S. Gales, D. L. Balabanski, F. Negoita, O. Tesileanu, C. A. Ur, D. Ursescu, and N. V. Zamfir, *Phys. Scr.* **91**, 093004 (2016).
 - [6] I.C.E. Turcu, F. Negoita, D.A. Jaroszynski, P. McKenna, S. Balascuta, D. Ursescu, I. Dancus, M.O. Cernaianu, M.V. Tataru, P. Ghenuche, et al., *Rom. Rep. Phys.* **68**, S145 (2016).
 - [7] K. L. Seong, H. T. Kim, I. W. Choi, C. M. Kim, and C.-H. Nam, *Journal of the Korean Physical Society* **73**, 179 (2018).
 - [8] S. Singh, R. Versaci, A. Laso Garcia, L. Morejon, A. Ferrari, M. Molodtsova, R. Schwengner, D. Kumar, and T. Cowan, *Review of Scientific Instruments* **89**, 085118 (2018).
 - [9] R. L. Clough, *Nucl. Instr. Meth. Res. B*, **185**, 8 (2001).
 - [10] A. G. Chmielewski, M. Haji-Saeid, and S. Ahmed, *Nucl. Instr. Meth. Res. B*, **236**, 44 (2005).
 - [11] G. Lowenthal and P. Airey, *Practical Applications of Radioactivity and Nuclear Radiations* (Cambridge Univer-

- sity Press, Cambridge, England, 2001)
- [12] J. C. Ganz, *Gamma Knife Neurosurgery* (Springer-Verlag, Wien, 2011).
- [13] F. Albert, S. G. Anderson, G. A. Anderson, S. M. Betts, D. J. Gibson, C. A. Hagmann, J. Hall, M. S. Johnson, M. J. Messerly, V. A. Semenov, M. Y. Shverdin, A. M. Tremaine, F. V. Hartemann, C. W. Siders, D. P. McNabb, and C. P. J. Barty, *Optics Letters*, **35**, No. 3 (2010).
- [14] S. V. Bulanov, T. Zh. Esirkepov, M. Kando, J. Koga, K. Kondo, and G. Korn, *Plasm. Phys. Rep.* **41**, 1 (2015).
- [15] M. J. Rees and R. Mészáros, *Mon. Not. R. Astr. Soc.* **258**, 41 (1992).
- [16] T. Piran, *Mod. Phys.* **76**, 1143 (2005).
- [17] A. A. Philippov and A. Spitkovsky, *ApJ*, **855**, 94 (2018).
- [18] T. Nakamura, J. K. Koga, T. Zh. Esirkepov, M. Kando, G. Korn, and S. V. Bulanov, *Phys. Rev. Lett.* **108**, 195001 (2012).
- [19] C. P. Ridgers, C. S. Brady, R. Duclous, J. G. Kirk, K. Bennett, T. D. Arber, A. P. L. Robinson, and A. R. Bell, *Phys. Rev. Lett.* **108**, 165006 (2012).
- [20] S. V. Bulanov, T. Zh. Esirkepov, M. Kando, J. K. Koga, T. Nakamura, S. S. Bulanov, A. G. Zhidkov, Y. Kato, and G. Korn, *Proceedings of SPIE-2013 International Conference, 15-18 April, Prague, Czech Republic. SPIE Optics+ Optoelectronics*, 878015-878015-15 (2013).
- [21] X. L. Zhu, T. P. Yu, Z. M. Sheng, Y. Yin, I. C. E. Turcu, and A. Pukhov, *Nat. Communications* **7**, 13686 (2016).
- [22] M. Vranic, T. Grismayer, R. A. Fonseca, and L. O. Silva, *Plasma Phys. Control. Fusion* **59**, 014040 (2016).
- [23] Z. Gong, R. H. Hu, Y. R. Shou, B. Qiao, C. E. Chen, X. T. He, S. S. Bulanov, T. Zh. Esirkepov, S. V. Bulanov, X. Q. Yan, *Phys. Rev. E* **95**, 013210 (2017).
- [24] H.-Z. Li, T.-P. Yu, J.-J. Liu, Y. Yin, X.-L. Zhu, R. Capdessus, F. Pegoraro, Z.-M. Sheng, P. McKenna, and F.-Q. Shao, *Sci. Reports* **7**, 17312 (2017).
- [25] R. Capdessus, M. King, D. Del Sorbo, M. Duff, C. P. Ridgers, and P. McKenna, *Sci. Reports* **7**, 9155 (2018).
- [26] A. Benedetti, M. Tamburini, and C. H. Keitel, *Nature Photonics* **12**, 319323 (2018).
- [27] A. Macchi, F. Pegoraro, *Nature Photonics* **12**, 314315 (2018).
- [28] O. Jansen, T. Wang, D. J. Stark, E. d’Humières, T. Toncian, and A. V. Arefiev, *Plasma Phys. Control. Fusion* **60**, 054006 (2018).
- [29] C. P. Ridgers, J. G. Kirk, R. Duclous, T. G. Blackburn, C. S. Brady, K. Bennett, T. D. Arber, and A. R. Bell, *J. Comput. Phys.* **260**, 273 (2014).
- [30] A. Di Piazza, C. M. Müller, K. Z. Hatsagortsyan, and C. H. Keitel, *Rev. Mod. Phys.* **84**, 1177 (2012).
- [31] S.-Y. Chen, A. Maksimchuk, and D. Umstadter, *Nature* **396**, 653 (1998).
- [32] G. Sarri, D. J. Corvan, W. Schumaker, J. M. Cole, A. Di Piazza, H. Ahmed, C. Harvey, C. H. Keitel, K. Krushelnick, S. P. D. Mangles, Z. Najmudin, D. Symes, A. G. R. Thomas, M. Yeung, Z. Zhao, and M. Zepf, *Phys. Rev. Lett.* **113**, 224801 (2014).
- [33] W. Yan, C. Fruhling, G. Golovin, D. Haden, J. Luo, P. Zhang, B. Zhao, J. Zhang, C. Liu, M. Chen, S. Chen, S. Banerjee, and D. Umstadter, *Nat. Photonics* **11**, 514520 (2017).
- [34] L. A. Gizzi, D. Giulietti, A. Giulietti, P. Audebert, S. Bastiani, J. P. Geindre, and A. Mysyrowicz, *Phys. Rev. Lett.* **76**, 2278 (1996).
- [35] J. Galy, M. Maucec, D. J. Hamilton, R. Edwards, J. Magill, *New J. Phys.* **9**, 23 (2007).
- [36] C. Courtois, A. Compant La Fontaine, O. Landoas, G. Lidove, V. Méot, P. Morel, R. Nuter, E. Lefebvre, A. Boscheron, J. Grenier, M. M. Aléonard, M. Gerbaux, F. Gobet, F. Hannachi, G. Malka, J. N. Scheurer, and M. Tarisien, *Phys. Plasmas* **16**, 013105 (2009).
- [37] A. Henderson, E. Liang, N. Riley, P. Yepes, G. Dyer, K. Serratto, and P. Shagin, *High Energy Density Physics* **12**, 46 (2014).
- [38] J. Vyskocil, O. Klimo, and S. Weber, *Plasma Phys. Controlled Fusion* **60**, 054013 (2018).
- [39] D. Wu, W. Yu, Y. T. Zhao, S. Fritzsche, and X. T. He, *Matter and Radiation at Extremes* (2018).
- [40] V. B. Berestetskii, E. M. Lifshitz, and L. P. Pitaevskii, *Quantum Electrodynamics* (Pergamon, Oxford, 1982).
- [41] C. Bula, K. T. McDonald, E. J. Prebys, C. Bamber, S. Boege, T. Kotseroglou, A. C. Melissinos, D. D. Meyerhofer, W. Ragg, D. L. Burke, R. C. Field, G. Horton-Smith, A. C. Odian, J. E. Spencer, D. Walz, S. C. Berridge, W. M. Bugg, K. Shmakov, and A. W. Weidemann, *Phys. Rev. Lett.* **76**, 3116 (1996).
- [42] F. Ehlötzky, K. Krajewska, and J. Z. Kaminski, *Rep. Prog. Phys.* **72**, 046401 (2009).
- [43] L. D. Landau and E. M. Lifshitz, *The Classical Theory of Fields* (Pergamon, Oxford, 1980).
- [44] M. Marklund and P. Shukla, *Rev. Mod. Phys.* **78**, 591 (2006).
- [45] T. Zh. Esirkepov, J. K. Koga, A. Sunahara, T. Morita, M. Nishikino, K. Kageyama, H. Nagatomo, K. Nishihara, A. Sagisaka, H. Kotaki, T. Nakamura, Y. Fukuda, H. Okada, A. S. Pirozhkov, A. Yogo, M. Nishiuchi, H. Kiriya, K. Kondo, M. Kando, and S. V. Bulanov, *Nucl. Instrum. Methods Phys. Res. Sect. A* **745**, 150 (2014).
- [46] D. Margarone, A. Velyhan, J. Dostal, J. Ullschmied, J. P. Perin, D. Chatain, S. Garcia, P. Bonny, T. Pisarczyk, R. Dudzak, M. Rosinski, J. Krasa, L. Giuffrida, J. Prokuper, V. Scuderi, J. Psikal, M. Kucharik, M. De Marco, J. Cikhardt, E. Krousky, Z. Kalinowska, T. Chodukowski, G. A. P. Cirrone, and G. Korn, *Phys. Rev. X* **6**, 041030 (2016).
- [47] R. Duclous, J. G. Kirk, and A. R. Bell, *Plasma Phys. Controlled Fusion* **53**, 015009 (2011).
- [48] S. C. Wilks, A. B. Langdon, T. E. Cowan, M. Roth, M. Singh, S. Hatchett, M. H. Key, D. Pennington, A. MacKinnon, and R. A. Snavely, *Phys. Plasmas* **8**, 542 (2001).
- [49] T. Esirkepov, M. Borghesi, S. V. Bulanov, G. Mourou, and T. Tajima, *Phys. Rev. Lett.* **92**, 175003 (2004).
- [50] S. V. Bulanov, M. Lontano, T. Zh. Esirkepov, F. Pegoraro, and A. M. Pukhov, *Phys. Rev. Lett.* **76**, 3562 (1996).
- [51] S. S. Bulanov, V. Yu. Bychenkov, V. Chvykov, G. Kalinchenko, D. W. Litzenberg, T. Matsuoka, A. G. R. Thomas, L. Willingale, V. Yanovsky, K. Krushelnick, and A. Maksimchuk, *Phys. Plasmas* **17**, 043105 (2010).
- [52] J. Koga, T. Zh. Esirkepov, and S. V. Bulanov, *Phys. Plas.* **12**, 093106, (2005).
- [53] F. Mackenroth, N. Kumar, N. Neitz, and C. H. Keitel, *arXiv preprint arXiv:1805.01762*, 2018.
- [54] A. I. Akhiezer and R. V. Polovin, *Sov Phys. JETP* **30**, 915 (1956).
- [55] D. E. Cullen, M. H. Chen, J. H. Hubbell, S. T. Perkins, E. F. Plechaty, J. A. Rathkopf, and J. H. Scofield. *Tables*

and graphs of photon-interaction cross sections from 10

eV to 100 GeV derived from the LLNL Evaluated Photon Data Library (EPDL). United States: N. p., 1989.